Hybrid Machine Learning Forest Height Estimation From TanDEM-X InSAR

Islam Mansour, *Member, IEEE*, Konstantinos Papathanassiou, *Fellow, IEEE*, Ronny Hänsch, *Senior Member, IEEE*, and Irena Hajnsek, *Fellow, IEEE*

***Abstract*— Combining machine learning (ML) with physical models can significantly impact retrieval algorithms designed to invert geophysical parameters from remote sensing data. Such hybrid models integrate physical knowledge with domain expertise through a joint architecture, potentially enhancing performance by increasing the efficiency and flexibility of the physical model as well as the generalization and interpretability of the ML predictions. This work introduces a hybrid model for estimating forest height using single-baseline, single-polarization TanDEM-X interferometric coherence measurements. In this model, the vertical reflectivity profile is derived as a function of input features, including topographic and acquisition geometry descriptors, using a multilayer perceptron network. This profile is then used to invert forest height by leveraging the established physical relationship connecting the vertical reflectivity profile to forest height. The developed model is applied and validated on several TanDEM-X acquisitions over tropical sites with different acquisition geometries, and its performance is assessed against reference data derived from airborne LiDAR measurements.**

***Index Terms*— Forest height, forest height estimation, forest structure, hybrid modeling, InSAR, interferometry, machine learning (ML), physical modeling, remote sensing, synthetic aperture radar, TanDEM-X, temporal decorrelation, topographic effects.**

I. Introduction

ACCURATE measurements of forest height are relevant for forest inventory, forest disturbance, and carbon sequestration monitoring [1], [2], [3], [4], [5]. SAR interferometry, combined with polarimetric and/or spatial baseline diversity, is today one of the established remote sensing techniques for obtaining continuous forest height estimates of significant accuracy at large spatial scales. The related approaches are in first line model-based, exploring the inherent sensitivity of interferometric measurements to the 3D distribution of scatterers within forests. Model-based forest height inversion performance is well-understood and validated across various frequencies, from the X- to P-band, for different forest and terrain conditions [6], [7], [8], [9], [10], [11], [12]. The achieved performance critically depends on the definition of the inversion model, particularly the parameterization of the vertical reflectivity profile. While accurate and generic parameterization requires a certain number of parameters to be described, the constraint of achieving a balanced inversion model dictates the number of parameters needed to parameterize the vertical reflectivity profile to be matched by the number of available measurements. In the absence of a sufficient number of measurements, only oversimplified model parameterizations become possible, or ones constrained by overly strict assumptions, resulting in severely compromised performance as the model loses its ability to adapt to the underlying scattering.

A. ML Versus Physical Versus Hybrid Modeling

Both machine learning (ML) and deep learning (DL) approaches have been in the past years applied to various inverse remote sensing data problems with notable success. Data-driven ML and DL approaches are able to recognize patterns and relationships in multiparameter data spaces with high efficiency even when these are not apparent. They are particularly powerful when applied to parameter estimation problems where the underlying physical relationships are not established and/or lack a forward or inverse model description.

Following this trend, a number of ML and DL approaches have been proposed in recent years addressing the problem of forest height estimation from multiparameter SAR data alone or combined with other remote sensing datasets. The majority of them attempt to establish a direct relationship between the measured SAR parameters as backscatter intensities or interferometric coherences and forest height using supervised or unsupervised learning implementations [13], [14], [15], [16], [17], [18], [19], [20], [21], [22], [23], [24], [25].

However, although the achieved performance of such approaches is often impressive, their generalization and interpretability are rather limited especially in underdetermined inverse problems addressed with limited or even without prior knowledge and domain expertise. At the same time, pure data-driven approaches require large amount of reference data for a wide range of problem conditions that are often not available.

One way to overcome these disadvantages has been proposed in the context of physics-informed ML approaches

Received 31 July 2024; revised 1 November 2024; accepted 14 December 2024. Date of publication 19 December 2024; date of current version 3 January 2025. This work was supported by the DeepSAR Research Project, funded by Helmholtz AI under the Helmholtz Association of German Research Centers (HGF). *(Corresponding author: Islam Mansour.)*

Islam Mansour and Irena Hajnsek are with the Microwaves and Radar Institute, German Aerospace Center (DLR), 82234 Weßling, Germany, and also with the Chair of Earth Observation and Remote Sensing, Institute of Environmental Engineering, ETH Zürich, 8093 Zürich, Switzerland (e-mail: islam.mansour@dlr.de; irena.hajnsek@dlr.de).

Konstantinos Papathanassiou and Ronny Hänsch are with the Microwaves and Radar Institute, German Aerospace Center (DLR), 82234 Weßling, Germany (e-mail: kostas.papathanassiou@dlr.de; ronny.haensch@dlr.de).

Digital Object Identifier 10.1109/TGRS.2024.3520387

TABLE I
TANDEM-X DATASETS, SITES, SCENE ID'S, HOA [M], NOMINAL INCIDENCE ANGLE [°]

No	Site	Scene ID	HoA	θ_0
1	Lopé	TDM1_SAR__COS_BIST_SM_S_SRA_20190610T173107_20190610T173115	52.45	46.18
2	Lopé	TDM1_SAR__COS_BIST_SM_S_SRA_20160125T173041_20160125T173048	-65.22	44.44
3	Lopé	TDM1_SAR__COS_BIST_SM_S_SRA_20111002T045625_20111002T045633	86.34	46.08
4	Lopé	TDM1_SAR__COS_BIST_SM_S_SRA_20121226T045626_20121226T045634	94.89	45.10
5	Lopé	TDM1_SAR__COS_BIST_SM_S_SRA_20121215T045627_20121215T045635	95.41	46.68
6	Mabounié	TDM1_SAR__COS_BIST_SM_S_SRA_20161017T050537_20161017T050545	-80.30	37.07
7	Mabounié	TDM1_SAR__COS_BIST_SM_S_SRA_20161017T050530_20161017T050538	-80.90	37.09
8	Mabounié	TDM1_SAR__COS_BIST_SM_S_SRA_20161028T050538_20161028T050546	-87.32	39.30
9	Mabounié	TDM1_SAR__COS_BIST_SM_S_SRA_20161108T050538_20161108T050546	-95.81	41.39
10	Rabi	TDM1_SAR__COS_BIST_SM_S_SRA_20161017T050558_20161017T050606	-78.51	37.04
11	Rabi	TDM1_SAR__COS_BIST_SM_S_SRA_20161028T050559_20161028T050607	-85.27	39.24
12	Rabi	TDM1_SAR__COS_BIST_SM_S_SRA_20161028T050552_20161028T050600	-85.95	39.27
13	Rabi	TDM1_SAR__COS_BIST_SM_S_SRA_20161108T050552_20161108T050600	-94.21	41.37

that integrate ML and physical/mathematical models [26]. This allows to combine the expressiveness of data-based approaches with the interpretability and generalization of physical models. In this context, this study attempts to establish such a hybrid inversion framework, which combines ML and physical modeling components for the estimation of forest height from single-baseline single-polarimetric TanDEM-X interferometric coherence. For this, the vertical reflectivity profile is derived as a function of input features, including topographic and acquisition geometry descriptors, using a multilayer perceptron network. In a second step, the predicted vertical reflectivity profile is used to invert forest height taking advantage of the established physical relationship connecting the vertical reflectivity profile to forest height.

The hybrid modeling approach is expected: 1) to use the capability of ML techniques in identifying nonobvious relationships or correlations, such as change in scattering behavior with terrain topography and 2) to take advantage of the well-established physical models to restrict the possible solution space down to physically meaningful solutions, making the training process more efficient and reducing the diversity of training data required (as for example the need for reference data at different terrain conditions).

This article is structured as follows: Section II introduces the data used in this work, Section III provides the technical background required, Section IV presents the proposed hybrid model and describes its implementation, Section V discusses the results obtained when applying the proposed hybrid model to TanDEM-X acquisitions, and finally, Section VI draws the conclusions.

II. STUDY AREA AND EXPERIMENTAL DATA

This study uses data from three Gabonese tropical forest sites: Lopé, Mabounié, and Rabi. The Lopé site is within the Lopé National Park, consisting of Savannah and denser forest of varying species composition and density. The maximum tree height exceeds 50 m in many stands. The terrain is hilly, with many local slopes steeper than 20°. Mabounié is a former mining exploration site. Most of the test site is covered by mature primary forest stands (with tree heights between 40 and 50 m) and degraded forest (with tree heights around 20 m). The terrain is relatively flat with few gentle slopes. Finally, the Rabi test site consists of a diverse mix of upland and wet forest with a mean tree height of about 40 m and features fairly flat topography.

A large set of TanDEM-X images acquired over the three sites is used. Table I summarizes the acquisitions and their geometry. The (2π) height of ambiguity (HoA) sign indicates the orbit direction: a positive sign indicates an ascending orbit, while a negative sign indicates a descending orbit.

Full-waveform LiDAR data were collected during the AfriSAR2016 campaign in February 2016 by NASA's airborne Land, Vegetation, and Ice Sensor (LVIS) LiDAR sensor. The LVIS footprints range from 18 to 22 m, and the waveforms were resampled to a regular 20 × 20 m grid with the corresponding RH98 and DTM models [27], [28]. The resampled RH98 heights are used as the reference heights $h_{\mathrm{Ref}} = \mathrm{RH98}$.

III. METHODOLOGY

The measured interferometric coherence ($\tilde{\gamma}_{\mathrm{obs}}$) between two interferometric images $s_1(\vec{w})$ and $s_2(\vec{w})$ acquired at a given polarization $\vec{w}$ is expressed as follows [29], [30]:

$$\tilde{\gamma}_{\mathrm{obs}}(\kappa_z, \vec{w}) = \frac{\langle s_1(\vec{w}) s_2^*(\vec{w}) \rangle}{\sqrt{\langle s_1(\vec{w}) s_1^*(\vec{w}) \rangle \langle s_2(\vec{w}) s_2^*(\vec{w}) \rangle}}. \quad (1)$$

The vertical wavenumber (in rad/m), κ_z, expresses the sensitivity of the interferometric phase to height changes [10], [31]

$$\kappa_z = m \frac{2\pi}{\lambda} \frac{\Delta\theta}{\sin(\theta_0 + \alpha)} \quad (2)$$

where θ_0 is the radar look angle, $\Delta\theta$ is the look angle difference induced by the spatial baseline, λ is the wavelength, and α is the ground range terrain slope. The factor m depends on the interferometric acquisition mode: $m = 2$ for monostatic, while $m = 1$ for bistatic acquisitions. An equivalent way to express the sensitivity of the interferometric phase-to-height changes is the HoA $\mathrm{HoA} = 2\pi/\kappa_z$.

The measured interferometric coherence can be factorized as [32], [33], [34], [35]

$$\tilde{\gamma}_{\mathrm{obs}}(\kappa_z, \vec{w}) = \tilde{\gamma}_{\mathrm{Tmp}}(\vec{w}) \tilde{\gamma}_{\mathrm{Rg}}(\kappa_z) \tilde{\gamma}_{\mathrm{Sys}}(\vec{w}) \tilde{\gamma}_{\mathrm{Vol}}(\kappa_z, \vec{w}) \quad (3)$$

where $\widetilde{\gamma}_{\mathrm{Tmp}}(\vec{w})$ accounts for the temporal decorrelation, $\widetilde{\gamma}_{\mathrm{Rg}}(\kappa_z)$ accounts for the range spectral decorrelation induced by the spatial baseline, $\widetilde{\gamma}_{\mathrm{Sys}}(\vec{w})$ comprises various system-induced decorrelations, including the decorrelation due to the additive noise component, and finally, $\widetilde{\gamma}_{\mathrm{Vol}}(\kappa_z, \vec{w})$ is the decorrelation induced by the vertical extent of the scatterer.

In the case of bistatic TanDEM-X acquisitions, the factor m in (2) becomes 1 and the temporal decorrelation contribution $\widetilde{\gamma}_{\mathrm{Tmp}} = 1$. The system decorrelation contribution $\widetilde{\gamma}_{\mathrm{Sys}}$ and the range spectral decorrelation $\tilde{\gamma}_{\mathrm{Rg}}$ can be accurately estimated and compensated making an accurate estimation of the volume decorrelation $\widetilde{\gamma}_{\mathrm{Vol}}$ contribution possible [36], [37]. The measured interferometric coherence and several decorrelation contributions depend on the polarization of the images used to construct the interferogram. However, since polarimetric diversity is not considered in the following, the polarization dependence is omitted.

A. Vertical Reflectively Profile and Forest Height Inversion

The volume decorrelation contribution $\widetilde{\gamma}_{\mathrm{Vol}}(\kappa_z)$ is related to the vertical reflectivity profile $f(z)$ of the forest and its top canopy height h_v as [30], [38], [39]

$$\tilde{\gamma}_{\mathrm{Vol}}(\kappa_z) = e^{i\kappa_z z_o} \frac{\int_0^{h_v} f(z) e^{i\kappa_z z} dz}{\int_0^{h_v} f(z) dz} \tag{4}$$

where z denotes the position along the vertical axis. The vertical reflectivity profile $f(z)$ represents the vertical distribution of scatterers and as such depends on the frequency, polarization, and acquisition geometry. The lower boundary of $f(z)$ is determined by the reference height z_0, which is related to the location of the underlying ground. The upper boundary of $f(z)$ is defined by $z_0 + h_v$.

In the case of TanDEM-X, only a single $\widetilde{\gamma}_{\mathrm{Vol}}(\kappa_z)$ measurement is available, at least for a very long-time interval, while the ground topography z_0, forest height h_v, and parameterization of the vertical reflectivity profile $f(z)$ have to be considered as unknowns.

B. Modeling Vertical Reflectivity Profiles

The vertical reflectivity profile can be expressed in terms of a polynomial series expansion. Originally, the Legendre polynomials were used for this [30], [40], [41], [42]

$$f(z, a_n) = \sum_{n=1}^{\infty} a_n P_n(z) \tag{5}$$

where $P_n(z)$ are the Legendre polynomials (Fig. 1) and a_n are the associated Legendre coefficients that are obtained as

$$a_n = \frac{2n+1}{2} \int_{-1}^{1} f(z) P_n(z) dz. \tag{6}$$

The summation extends to infinity, although, in practice, it is truncated to a small number of terms. The proposed Legendre polynomials have proven to be a well-suited generic basis as they allow accurate reconstruction of $f(z, a_n)$ with a small number of polynomials for various forest conditions.

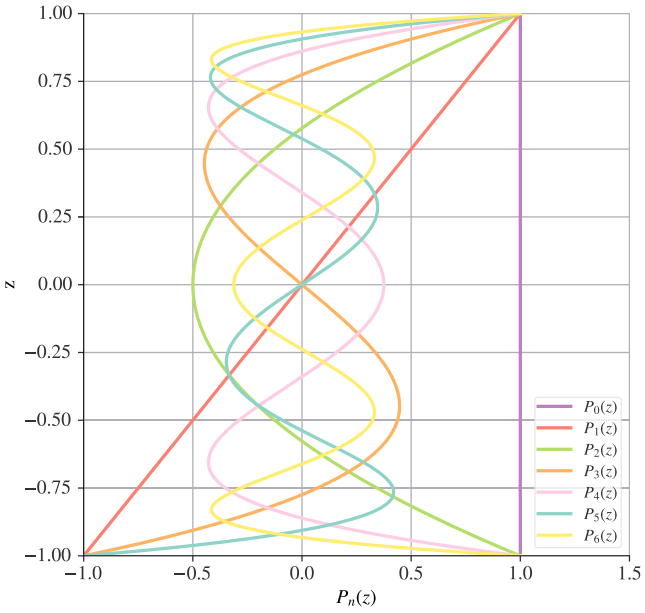

Fig. 1. Graphical illustration showcasing the initial seven Legendre polynomials plotted as a function of x, highlighting their distinct properties and orthogonality within the given domain.

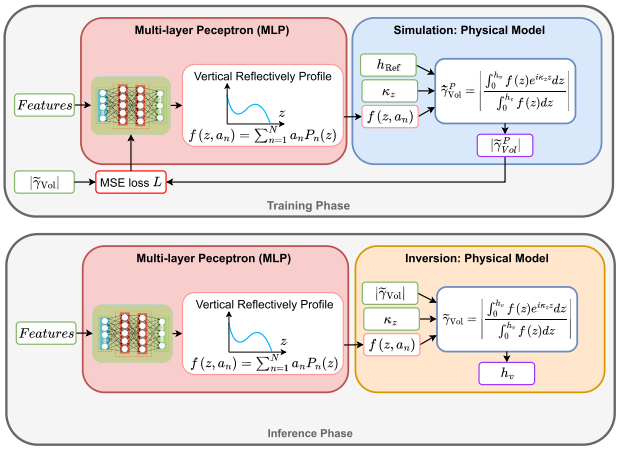

Fig. 2. Conceptual architecture and functionality of the hybrid model in (top) training phase and (bottom) inference phase.

IV. Model Definition

The proposed hybrid model uses an ML algorithm to predict the underlying vertical reflectivity profile $f(z, a_n)$, expressed in terms of the Legendre series expansion [(5)], as a function of features including interferometric volume coherence, acquisition geometry (expressed by the vertical wavenumber), and terrain slope. The predicted (or "learned") vertical reflectivity profile $f(z, a_n)$ is then used in the inversion of (4) to estimate the forest height. Fig. 2 shows a conceptual representation of the architecture and functionality of the proposed hybrid model in the training and inference phases.

A. Model Training

In the training phase, the terrain-corrected vertical wavenumber [(2)] and the reference forest height h_{Ref} are used

in (4) to predict the absolute value of the volume decorrelation $|\widetilde{\gamma}^{P}_{\mathrm{Vol}}(\kappa_z, h_{\mathrm{Ref}}, f(z,a_n))|$ for a given vertical reflectivity profile $f(z,a_n)$ expressed by a predefined number ($N=3$ or $N=7$) of Legendre polynomials using the associated coefficients a_n [(6)]. The obtained volume decorrelation prediction is then compared against the volume decorrelation $|\widetilde{\gamma}_{\mathrm{Vol}}(\kappa_z)|$ as estimated from the TanDEM-X data.

The training process begins with an arbitrary initialization of the Legendre coefficients a_n. The coefficients are then iteratively updated to minimize the difference between the predicted and actual volume decorrelation values. The coefficients are determined by a multilayer perceptron to establish the nonlinear relationship between them and the set of input features by minimizing the difference between the predicted and estimated volume decorrelation values. The set of input features includes the terrain corrected vertical wavenumber κ_z, the volumetric coherence $|\widetilde{\gamma}_{\mathrm{Vol}}(\kappa_z)|$, the incidence angle to the ellipsoid corresponding to the angle between the line-of-sight and the normal to the local ellipsoid θ_0, the local incidence angle θ_{loc}, and the terrain slope in the range direction α. The optimization process uses a suitable loss function mean-squared error (mse) and the Adam optimization algorithm [43]

$$\mathcal{L}\left(\widetilde{\gamma}^{P}_{\mathrm{Vol}}, \widetilde{\gamma}_{\mathrm{Vol}}\right) = \sum_{i=1}^{m}\left(\left|\widetilde{\gamma}^{P}_{\mathrm{Vol}}(\kappa_z, h_{\mathrm{Ref}}, f(z,a_n))\right| - \left|\widetilde{\gamma}_{\mathrm{Vol}}(\kappa_z)\right|\right)^2 \tag{7}$$

subject to

$$f(z,a_n) = \sum_{n=1}^{N} a_n\left(\kappa_z, \left|\widetilde{\gamma}_{\mathrm{Vol}}\right|, \theta, \theta_{\mathrm{loc}}, \alpha\right) P_n(z). \tag{8}$$

This way the model enhances its ability to link the features and the Legendre coefficients of the vertical reflectivity profile.

An important point is to constrain positive reflectivity profiles to ensure physically plausible vertical reflectivity functions. To enforce positive profiles, a hyperbolic tangent activation function is incorporated. Furthermore, to ensure the physical plausibility of the model predictions, a linear (regression) layer with a MinMaxNorm kernel constraint is also integrated to constrain the weights of the model within a certain range

$$\sum_{n=1}^{N} a_n\left(\kappa_z, \left|\widetilde{\gamma}_{\mathrm{Vol}}(\kappa_z)\right|, \theta, \theta_{\mathrm{loc}}, \alpha\right) P_n(z) \geq 0. \tag{9}$$

For $n = 1, 2, 3, \ldots, N$ and $0 \leq h_v \leq h_{\max}$, where $h_{\max}$ is set to 70. This constraint ensures that the predicted vertical reflectivity profiles are positive and fall within a reasonable range.

B. Model Inversion

Once the model is trained, it can be used to estimate forest height from the input features. In a first step, the input features are used to predict the vertical reflectivity profile $f(z,a_n)$, which is subsequently used to estimate the forest height from the $|\widetilde{\gamma}_{\mathrm{Vol}}(\kappa_z)|$ measurements in terms of (4). This last step can be implemented in terms of a lookup table.

TABLE II

MODELS AND ASSOCIATED NUMBER OF LEGENDRE COEF. AND TANDEM-X ACQUISITION(S) AND HOA USED FOR TRAINING [AS SHOWN IN FIG. 2 (TOP)]

Model	Coef.	HoA (m)	ML Input Features	PM Inputs
A	3	-65.22 (No 2 in Table I)	κ_z, $\lvert\widetilde{\gamma}_{\mathrm{Vol}}(\kappa_z)\rvert$, θ, θ_{loc}, α	h_{Ref}, κ_z, $f(z,a_n)$
B	3	52.45 (No 1 in Table I) -65.22 (No 2 in Table I) 95.41 (No 5 in Table I)	κ_z, $\lvert\widetilde{\gamma}_{\mathrm{Vol}}(\kappa_z)\rvert$, θ, θ_{loc}, α	h_{Ref}, κ_z, $f(z,a_n)$
C	7	52.45 (No 1 in Table I) -65.22 (No 2 in Table I) 95.41 (No 5 in Table I)	κ_z, $\lvert\widetilde{\gamma}_{\mathrm{Vol}}(\kappa_z)\rvert$, θ, θ_{loc}, α	h_{Ref}, κ_z, $f(z,a_n)$

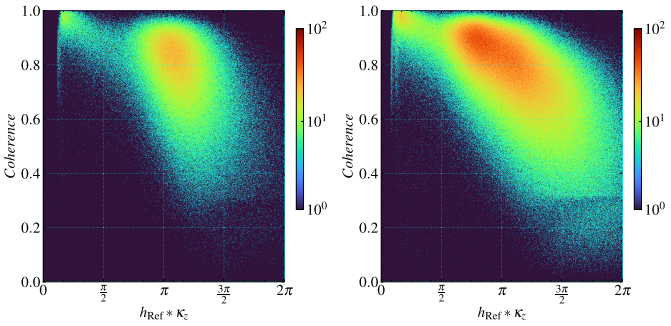

Fig. 3. Volume coherence $|\widetilde{\gamma}_{\mathrm{Vol}}(\kappa_z)|$ versus $h_{\mathrm{Ref}}\kappa_z$ for the data space available for training when (left) one, the No. 2 in Table I, or (right) three, the No. 1, 2, and 5 in Table I, TanDEM-X acquisitions are used. The colors represent the relative sample density, ranging from dark blue (low density) to dark red (high density).

Note that the interferometric volume coherences used for training and inversion are derived from the interferometric coherences estimated using a 7×7 window estimator as described in [10].

C. Model Implementation

Three different models have been developed, differing in the number and range of vertical wavenumbers (e.g., number of TanDEM-X acquisitions) used for training and in the number of Legendre polynomials used for the definition of the vertical reflectivity profiles. The three models are summarized in Table II. The first model (A) was trained using a single TanDEM-X acquisition and used three Legendre polynomials ($N=3$) to define the vertical reflectivity profiles. The second model (B) was trained using three TanDEM-X acquisitions (two ascending and one descending) with different vertical wavenumbers and three Legendre polynomials ($N=3$) for the definition of the vertical reflectivity profiles. Finally, the third model (C) also used three TanDEM-X acquisitions for training (the same as for model B) but seven Legendre polynomials ($N=7$) for defining the vertical reflectivity profiles. For each of the three models, the available reference data were split such that 60% of the data were used for training and 40% for validation.

The data space available for training in the case of using one (as in model A) or three (as in models B and C) TanDEM-X acquisitions is shown in Fig. 3. There, the estimated volume

coherence $|\widetilde{\gamma}_{\mathrm{Vol}}(\kappa_z)|$ for the one (on the left) and the three (on the right) TanDEM-X acquisitions used for training are plotted against the product $h_{\mathrm{Ref}}\kappa_z$, i.e., the product of the (terrain corrected) vertical wavenumber κ_z with the reference forest height h_{Ref} for each sample in the scene. The increased training space when using three TanDEM-X acquisitions is evident.

For training, acquisitions with (very) different vertical wavenumbers are ideal to provide maximum coherence contrast. And, of course, acquisitions with vertical wavenumbers similar to those targeted for inversion are likely to yield better inversion performance. In this study, an acquisition with moderately different vertical wavenumbers and one acquisition in opposite geometry (descending) were preferred to avoid overly optimistic inversion performance, thereby highlighting both the strengths and remaining limitations of the proposed approach.

V. Results and Discussion

The three established models are applied to the TanDEM-X dataset and validated against the available reference heights. The validation focuses on assessing the inversion performance by considering the number and range of vertical wavenumbers (e.g., TanDEM-X acquisitions) used in the training phase and the number of Legendre polynomials used for the definition of the reflectivity profiles. First, the performance obtained when training and inversion occur on the same site, but for different acquisitions, is discussed. For this case, the Lopé site is chosen. In a second step, the performance obtained when the Lopé model is applied to the other two sites, Mabounié and Rabi, for which it has not been trained, is evaluated.

The performance achieved over the Lopé site is summarized in the three Figs. 4–6. Fig. 4 shows the vertical reflectivity profiles "learned" by the three models, A (top), B (middle), and C (bottom), for different terrain slopes. In the absence of a direct way to assess the correctness of the vertical reflectivity profiles "learned" by the models, their slope dependence is one of the few, if not the only, test that allows some conclusions about their physical credibility.

Indeed, the ability of the model to predict a stronger ground scattering contribution on positive slopes facing toward the radar than on negative slopes facing away is consistent with the physical anticipation and thus an indication for the credibility of the "learned" vertical reflectivity profiles. The light shadow colors indicate the variance of the profiles within each slope interval to illustrate the significance of the terrain adaptation provided by the ML component. With increasing number of acquisitions used for training the terrain adaptation improves as indicated by the smaller profile variance of models B and C with respect to model A. In addition, the improved vertical resolution as the number of polynomials increases from three to seven is evident when comparing the three models. From models A to C, there is a more detailed definition of the different layers of the vertical structure of the canopy.

Fig. 5 shows the plots obtained by plotting the volume coherence $|\widetilde{\gamma}_{\mathrm{Vol}}(\kappa_z)|$ against the product $h_v\kappa_z$ for each of the five TanDEM-X acquisitions and for each of the three models. From left to right, the plots corresponding to acquisitions

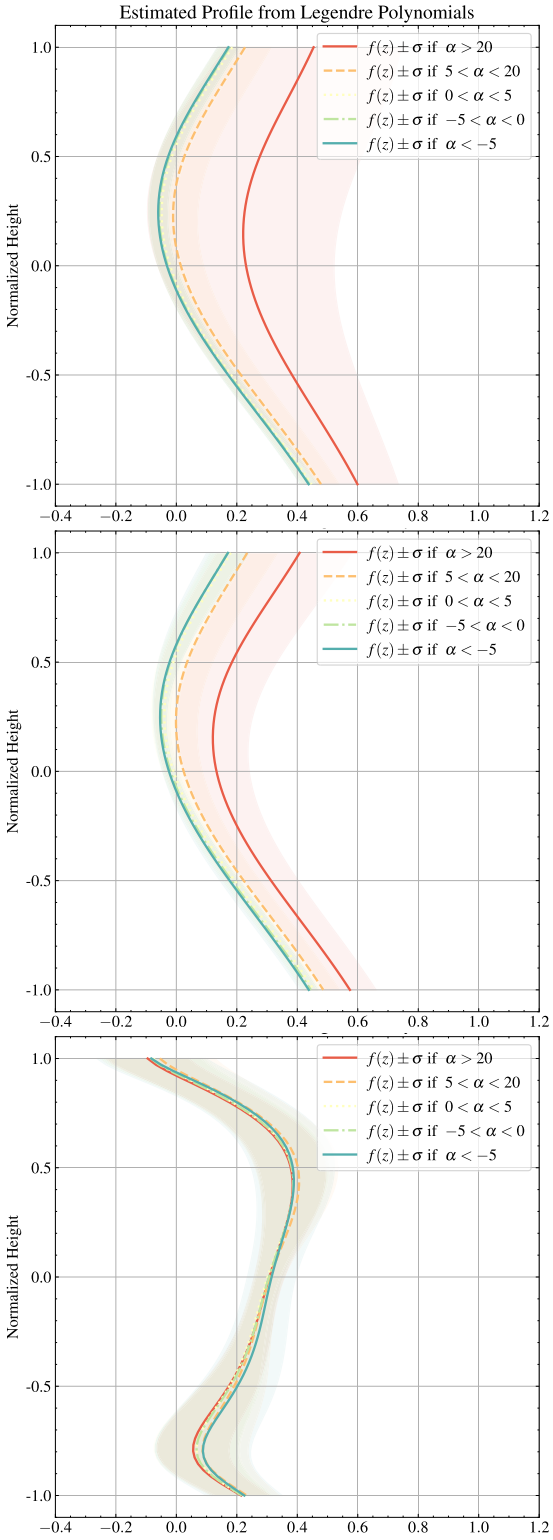

Fig. 4. Set of vertical reflectivity profiles "learned" by the three models, (top) A, (middle) B, and (bottom) C for different terrain slopes. Positive slopes facing toward the radar and are consistently estimated with a stronger ground scattering contribution than the profiles on negative slopes, which facing away. The light colors indicate the variance of the profiles within each slope interval.

1–5 (as referred to in Table I) are plotted. The forest height estimates in the top row are obtained from model A, in the middle from model B, and in the bottom row by using

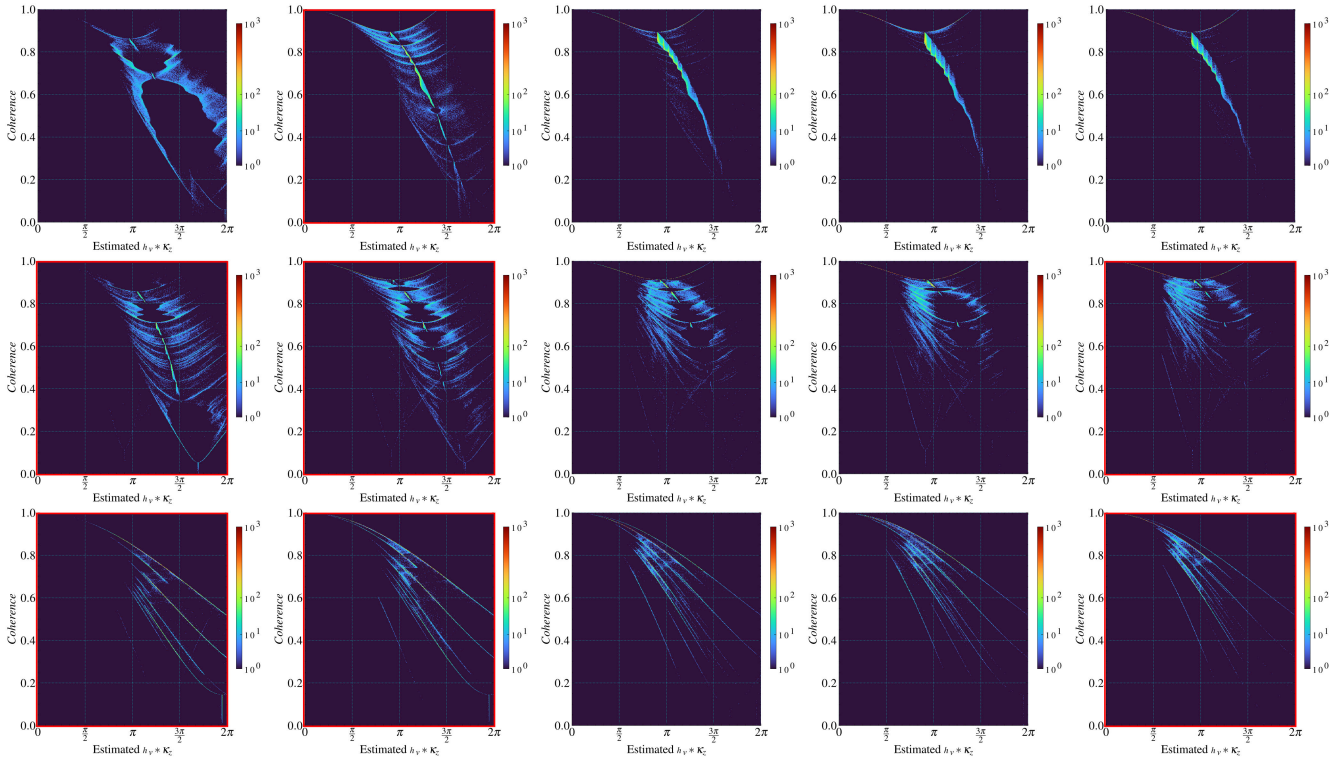

Fig. 5. $|\widetilde{\gamma}_{\mathrm{Vol}}(\kappa_z)|$ versus $h_v \kappa_z$ product. The plots are generated using the Lopé forest height estimates h_v obtained from the inversion of each of the five TanDEM-X acquisitions (from left to right acquisitions 1–5 according to their numbering in Table I) using the three models (A, B, and C from top to bottom). The framed plots indicate the acquisitions used for training. The colors represent the relative sample density, ranging from dark blue (low density) to dark red (high density).

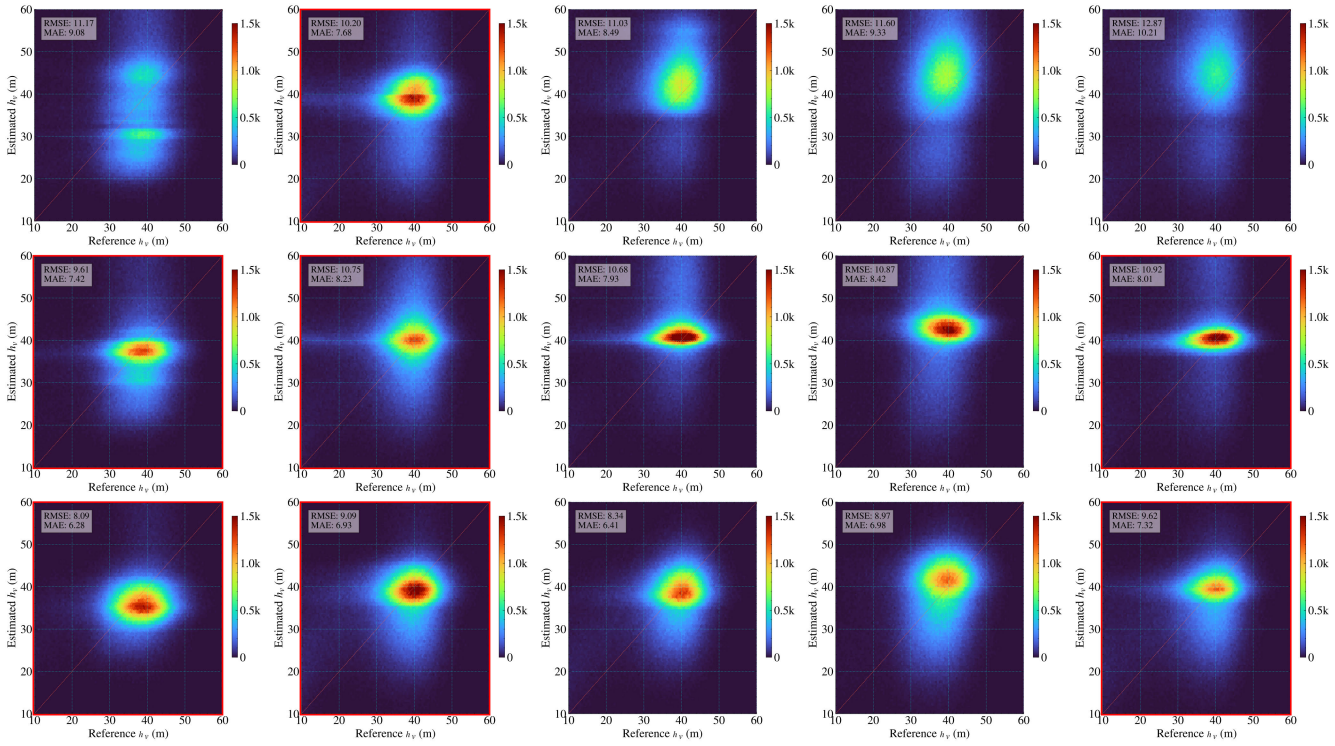

Fig. 6. Estimated h_v versus reference h_{Ref} forest height. The plots are generated using the Lopé forest height estimates h_v obtained from the inversion of each of the five TanDEM-X acquisitions (from left to right acquisitions 1–5 according to their numbering in Table I) using the three models (A, B, and C from top to bottom). The framed plots indicate the acquisitions used for training. The colors represent the relative sample density, ranging from dark blue (low density) to dark red (high density).

model C. The framed plots indicate the acquisitions used for training. Similarly, Fig. 6 shows the corresponding validation plots of the estimated forest height h_v for each of the five TanDEM-X acquisitions (1–5 from left to right, respectively)

plotted against the reference forest height h_{Ref}. The plots are arranged by model, with model A in the top row, model B in the middle row, and model C in the bottom row.

To better understand the results, we present the following figures that illustrate the model's performance across different scenarios.

The performance is characterized using the mean absolute error (MAE)

$$\mathrm{MAE} = \frac{1}{n}\sum_{i=1}^{n}\left|h_{vi} - h_{\mathrm{Ref}_i}\right| \tag{10}$$

and the root mean square error (RMSE)

$$\mathrm{RMSE} = \sqrt{\frac{1}{n}\sum_{i=1}^{n}\left(h_{vi} - h_{\mathrm{Ref}_i}\right)^2}. \tag{11}$$

In Fig. 5, each plot visualizes the solution space provided by the set of "learned" vertical reflectivity profiles for the corresponding TanDEM-X acquisition. Note that the set of "learned" vertical reflectivity profiles is intrinsic to each of the three models, i.e., the same set of learned profiles is used for each acquisition. Each "learned" vertical reflectivity profile $f(z, a_n)$ draws a unique curve in $|\tilde{\gamma}_{\mathrm{Vol}}(\kappa_z)|$ versus $h_v\kappa_z$ plane according to (4). In this sense, an optimal model should provide a set of "learned" vertical reflectivity profiles that are able to cover the whole data space in a unique way, and this over a wide range of vertical wavenumbers.

As can be seen, this is not the case for model A. While for the acquisition used for training, the set of "learned" vertical reflectivity profiles provides an acceptable coverage of the data space (i.e., compare with Fig. 3 left), this is not the case for all other acquisitions (e.g., vertical wavenumbers). Furthermore, for acquisition 1, the acquisition with the largest vertical wavenumber (e.g., smallest HoA), the solution space becomes ambiguous. This behavior directly reflects on the corresponding validation plots in Fig. 5 (top row), where unbiased results are obtained only for the acquisition used for training. For acquisitions 3–5 with larger HoA, the forest heights are overestimated, whereas for acquisition 1 with the smallest HoA the ambiguous solution space becomes evident. The MAE range is between 7.68 and 10.21 m, while the RMSE fluctuates between 10.20 and 12.87 m, as shown in Table III. Overall, model A has the highest mean errors among the three models, with an overall MAE of 8.89 m and an overall RMSE of 11.33 m, indicating its limited performance.

Model B performs better, as the "learned" vertical reflectivity profiles are able to cover almost the whole data space for all available acquisitions. There are only small data subspaces not covered by the solution space provided, as well as solution achieved at the ambiguous part of $h_v\kappa_z$ range, i.e., after reaching the first coherence minimum. These are indicators for a suboptimum set of "learned" vertical reflectivity profiles. However, this is not reflected on the performance plots (Fig. 6 middle) where the MAE values range between 7.42 and 8.42 m, and the RMSE values between 9.61 and 10.92 m, manifesting the improved performance compared with model A, as shown in Table III. Overall, model B achieves a lower mean MAE of 8.02 m and a mean RMSE of 10.58 m, indicating a notable performance improvement over model A.

TABLE III
PERFORMANCE COMPARISON OF DIFFERENT MODELS ACROSS SCENES BASED ON RMSE AND MAE METRICS

Scene No	Site	RMSE [m]	MAE [m]
Model A			
Scene 1	Lope	11.17	9.08
Scene 2	Lope	10.20	7.68
Scene 3	Lope	11.03	8.49
Scene 4	Lope	11.60	9.33
Scene 5	Lope	12.87	10.21
Overall		11.33	8.89
Model B			
Scene 1	Lope	9.61	7.42
Scene 2	Lope	10.75	8.23
Scene 3	Lope	10.68	7.93
Scene 4	Lope	10.87	8.42
Scene 5	Lope	10.92	8.01
Overall		10.58	8.02
Model C			
Scene 1	Lope	8.09	6.28
Scene 2	Lope	9.09	6.93
Scene 3	Lope	8.34	6.41
Scene 4	Lope	8.97	6.98
Scene 5	Lope	9.62	7.32
Overall		8.84	6.79

Finally, model C performs best, as the "learned" vertical reflectivity profiles are able to cover almost the whole data space in a consistent way across all available acquisitions. This is reflected also on its superior performance with lower MAE levels ranging from 6.28 to 7.32 m and lower RMSE levels ranging from 8.09 to 9.62 m, as summarized in Table III. Notably, model C achieves the lowest overall MAE and RMSE values among all models, with an overall MAE of 6.79 m and an overall RMSE of 8.84 m. Furthermore, the performance is very consistent across the entire range of vertical wavenumbers indicating the ability of the "learned" vertical reflectivity profiles to describe the underlying reflectivity.

In addition to the two cases using $N = 3$ (model B) and $N = 7$ (model C) Legendre coefficients to describe the vertical reflectivity profiles, models with varying N-values ranging from 3 to 9 were implemented and tested to assess their impact on inversion performance, consistently using the same three TanDEM-X acquisitions for training. The performance of models with $N = 4, 5$, and 6, as expected, lies between $N = 3$ and $N = 7$ cases, gradually improving with increasing N. For models with higher N values ($N = 8$ and 9), performance progressively deteriorates due to overfitting.

After evaluating the performance obtained when inverting acquisitions of the same area where training was performed but acquired with different vertical wavenumbers than the one(s) used for training, it is time to validate the transferability of the model to sites other than the one where it was trained. For this, the best performing model C is applied and validated on different TanDEM-X acquisitions over the Mabounié and Rabi sites. Both the sites are characterized by different forest types

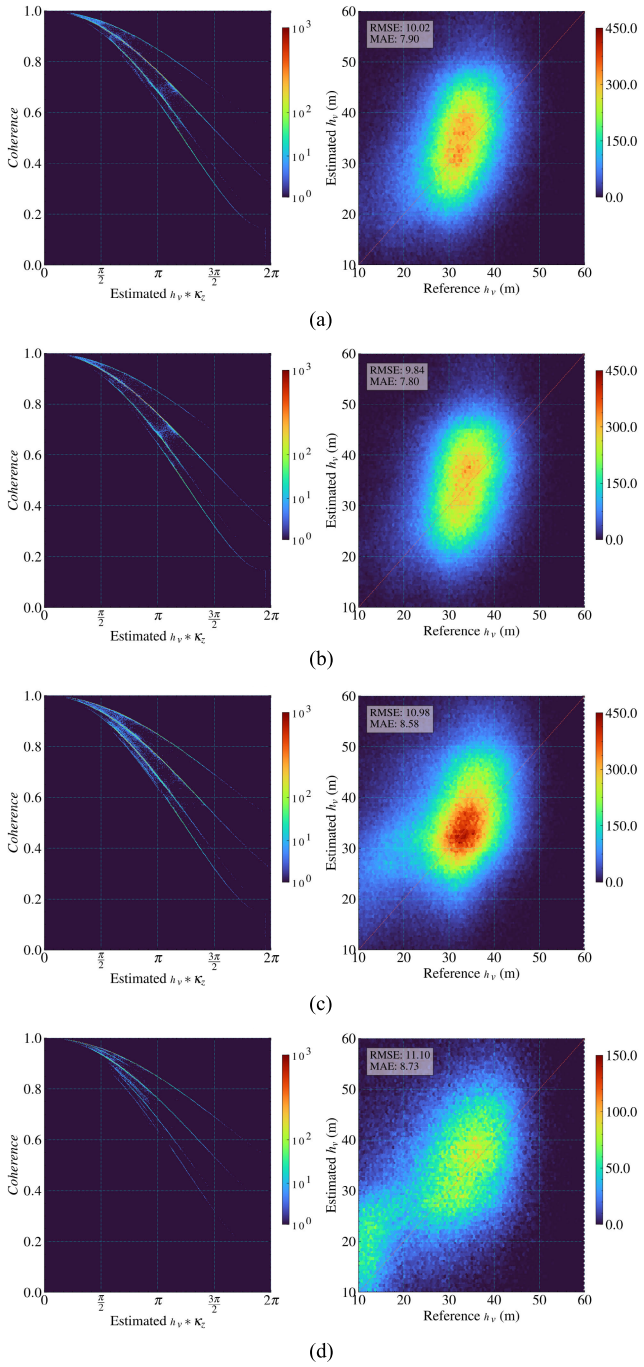

Fig. 7. (Left) Volume coherence $|\widetilde{\gamma}_{\text{Vol}}(\kappa_z)|$ versus $h_v\kappa_z$ plots and (right) validation plots for the four Mabounié acquisitions (from top to bottom acquisitions 6–9 according to their numbering in Table I). The colors represent the relative sample density, ranging from dark blue (low density) to dark red (high density). (a) Scene No. 6. (b) Scene No. 7. (c) Scene No. 8. (d) Scene No. 9.

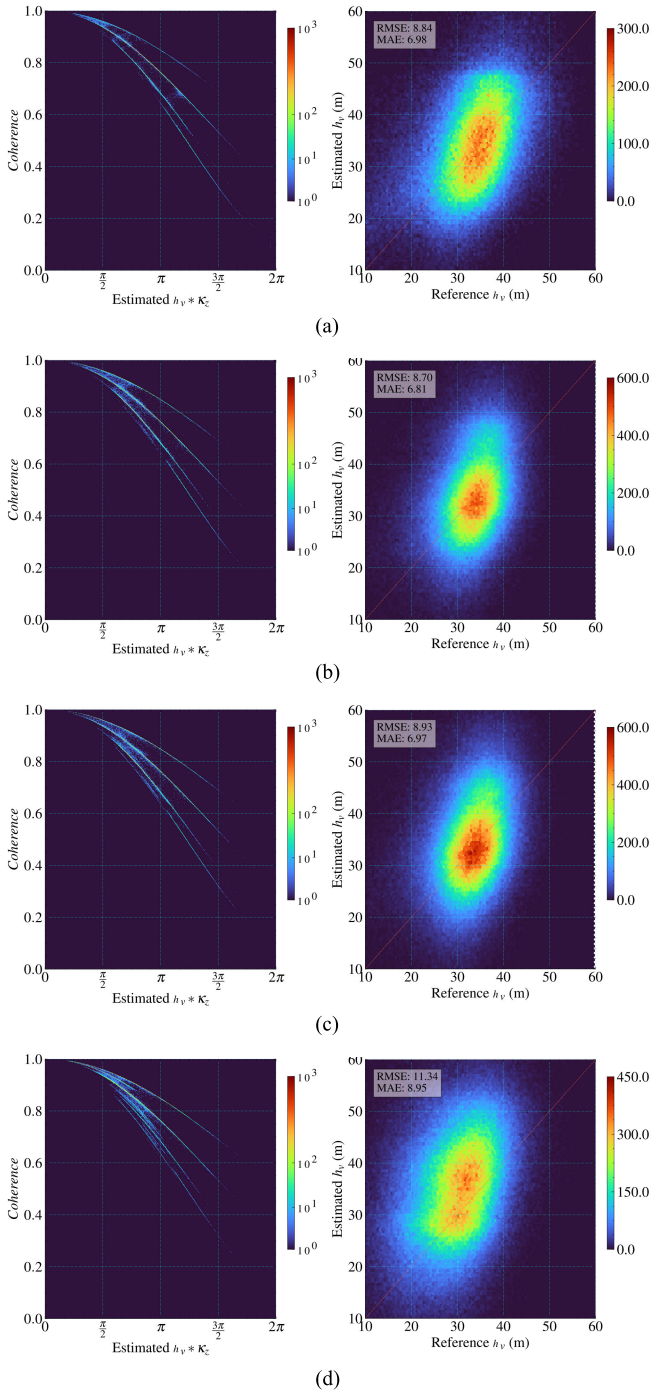

Fig. 8. (Left) Volume coherence $|\widetilde{\gamma}_{\text{Vol}}(\kappa_z)|$ versus $h_v\kappa_z$ plots and (right) validation plots for the four Rabi acquisitions (from top to bottom acquisitions 10–13 according to their numbering in Table I). The colors represent the relative sample density, ranging from dark blue (low density) to dark red (high density). (a) Scene No. 10. (b) Scene No. 11. (c) Scene No. 12. (d) Scene No. 13.

and forest height distributions and have different topographic characteristics than the Lopé site. The achieved results in form of the volume coherence $|\widetilde{\gamma}^{E}_{\text{Vol}}(\kappa_z)|$ versus $h_v\kappa_z$ plots and the validation plots are shown for the four Mabounié acquisitions (acquisitions 6–9 according to their numbering in Table I) in Fig. 7 and for the four Rabi acquisitions (acquisitions 10–13 according to their numbering in Table I) in Fig. 8. The plots are generated using the forest height estimates h_v obtained from the inversion of each of the TanDEM-X acquisitions.

The achieved performance is for all acquisitions on both the sites, as expected, inferior to the one achieved in Lopé. Looking on $|\widetilde{\gamma}_{\text{Vol}}(\kappa_z)|$ versus $h_v\kappa_z$ plots for both the sites, one sees that the vertical reflectivity profiles "learned" in Lopé are relevant enough to provide a consistent solution space for all Mabounié and Rabi acquisitions. However, comparing Lopé $|\widetilde{\gamma}_{\text{Vol}}\widetilde{\gamma}_{\text{Vol}}(\kappa_z)|$ versus $h_v\kappa_z$ plots (Fig. 5), it is also clear that only a subset of the "learned" reflectivity profiles are

TABLE IV
PERFORMANCE COMPARISON OF MODEL C ACROSS SITES BASED ON RMSE AND MAE METRICS

Scene No	Site	RMSE [m]	MAE [m]
Model C			
Scene 6	Mabounié	10.02	7.90
Scene 7	Mabounié	9.84	7.80
Scene 8	Mabounié	10.98	8.58
Scene 9	Mabounié	11.10	8.73
Scene 10	Rabi	8.84	6.98
Scene 11	Rabi	8.70	6.81
Scene 12	Rabi	8.93	6.97
Scene 13	Rabi	11.34	8.95

used for the inversion in Mabounié and Rabi. This is most likely because the reflectivity profiles "learned" in Lopé are not optimal to describe the underlying reflectivity in the other two sites due to the different forest structures there. The performance across the whole set of acquisitions (e.g., across the whole range of vertical wavenumbers) for both the sites is consistent and widely unbiased with MAE values ranging between 7.80 and 8.73 m and RMSE values between 9.84 and 11.10 m in Mabounié and with MAE values ranging between 6.81 and 8.95 m and RMSE values between 8.70 and 11.34 m in Rabi, as summarized in Table IV.

VI. CONCLUSION

In this study, a hybrid model combining ML with physical modeling was proposed for estimating forest height from single-baseline, single-polarimetric TanDEM-X interferometric coherence measurements. The integration of physical knowledge with domain expertise through a join architecture was attempted to improve the performance of the physical model and the interpretability of the ML architecture, resulting in an overall improved performance.

The proposed model uses an ML algorithm to predict the underlying vertical reflectivity profile, expressed in terms of the Legendre series expansion, as a function of features such as interferometric volume coherence, vertical wavenumber, and terrain slope. The predicted vertical reflectivity profile is then used in a physical relationship to estimate forest height.

Three different versions of such a hybrid model were implemented and applied to TanDEM-X acquisitions. The resulting forest heights were validated against the available reference heights. The emphasis was on assessing the inversion performance as a function of the number and the range of the vertical wavenumbers (e.g., TanDEM-X acquisitions) used in the training phase and the number of Legendre polynomials used to define the reflectivity profiles.

It appears that a certain vertical resolution of the vertical reflectivity profiles, expressed by the larger number of Legendre polynomials used to define them, is required to achieve better inversion performance. On the other hand, a set (e.g., more than one) of acquisitions with significantly different vertical wavenumbers are required to obtain vertical reflectivity profiles that are able to span a unique solution space covering the entire possible data space for a wide range of vertical wavenumbers. The best results in the study were obtained with three TanDEM-X acquisitions, but the important criterion is the difference in their vertical wavenumbers. With this in mind, two acquisitions may be sufficient for achieving acceptable performance. It is worth noting here that the combination of ascending and descending acquisitions in the training dataset appears to be possible.

The advantages of this approach are obvious. First, it allows forest height estimates to be obtained without the full observation space required for a model-based inversion. This is because the ML component seems to be able to establish a relationship between the shape of the vertical reflectivity profile and features such as interferometric volume coherence, the associated vertical wavenumber, and terrain topography. The advantages of the hybrid approach of first predicting a vertical reflectivity profile and then using it to perform a classical inversion are twofold: it minimizes the number of acquisitions required in the training phase to the few needed to "learn" the vertical reflectivity profile. The relationship between the interferometric volume coherence and the forest height at different vertical wavenumbers does not have to be established separately. It is given by the known vertical reflectivity profile.

The performance of any height estimation algorithm that uses interferometric coherence is critically dependent on its capacity to capture the spatial variation in the underlying reflectivity profile. This capability is strongly influenced by the boundary conditions of the inversion problem, such as the available observation space, the quantity and type of ancillary data or prior knowledge, and, importantly, the characteristics of the site where performance is evaluated. Consequently, comparing forest height estimation algorithms that operate under different boundary conditions is challenging. The proposed approach enables forest height estimation from a single TanDEM-X acquisition but, in its most effective implementation, requires three TanDEM-X acquisitions and a set of reference forest height measurements for training to account for the spatial variation in the underlying reflectivity profile.

Of course, the dependence of the vertical reflectivity profile on the different forest conditions is not trivial to be determined by any ML component, as it requires data and knowledge that are commonly not available. This lack of adaptability to the different forest structure conditions is also the main reason for the relatively high RMSE values characterizing the inversion results. This ability to adapt to local forest conditions remains the main advantage of model-based approaches, which—if the required observation space is available—are able to do so independently of the availability of any training datasets.

ACKNOWLEDGMENT

The authors would like to thank NASA Goddard Space Flight Center and the University of Maryland, College Park, MD, USA, for providing canopy metrics derived from the Land, Vegetation, and Ice Sensor (LVIS). They also like to thank the German Aerospace Center (DLR), Weßling, Germany, and the Leibniz Supercomputing Center (LRZ) for the computational and data resources provided by their joint High Performance Data Analysis (HPDA) project "terrabyte."

REFERENCES

[1] H. Pretzsch, "Forest dynamics, growth, and yield," in *Forest Dynamics, Growth and Yield: From Measurement to Model*, H. Pretzsch, Ed., Berlin, Germany: Springer, 2009, pp. 1–39.

[2] P. Köhler and A. Huth, "Towards ground-truthing of spaceborne estimates of above-ground life biomass and leaf area index in tropical rain forests," *Biogeosciences*, vol. 7, no. 8, pp. 2531–2543, Aug. 2010.

[3] M. Pause et al., "In situ/remote sensing integration to assess forest health—A review," *Remote Sens.*, vol. 8, no. 6, p. 471, Jun. 2016.

[4] B. S. Hardiman, G. Bohrer, C. M. Gough, C. S. Vogel, and P. S. Curtis, "The role of canopy structural complexity in wood net primary production of a maturing northern deciduous forest," *Ecology*, vol. 92, no. 9, pp. 1818–1827, Sep. 2011.

[5] G. Berndes et al., "Forest biomass, carbon neutrality and climate change mitigation," *Sci. Policy*, vol. 3, no. 7, pp. 1–27, Oct. 2016.

[6] J. Praks, F. Kugler, K. P. Papathanassiou, I. Hajnsek, and M. Hallikainen, "Height estimation of boreal forest: Interferometric model-based inversion at L- and X-band versus HUTSCAT profiling scatterometer," *IEEE Geosci. Remote Sens. Lett.*, vol. 4, no. 3, pp. 466–470, Jul. 2007.

[7] F. Garestier, P. C. Dubois-Fernandez, and I. Champion, "Forest height inversion using high-resolution P-band pol-InSAR data," *IEEE Trans. Geosci. Remote Sens.*, vol. 46, no. 11, pp. 3544–3559, Nov. 2008.

[8] F. Garestier, P. C. Dubois-Fernandez, and K. P. Papathanassiou, "Pine forest height inversion using single-pass X-band PolInSAR data," *IEEE Trans. Geosci. Remote Sens.*, vol. 46, no. 1, pp. 59–68, Jan. 2008.

[9] I. Hajnsek, F. Kugler, S.-K. Lee, and K. P. Papathanassiou, "Tropical-forest-parameter estimation by means of Pol-InSAR: The INDREX-II campaign," *IEEE Trans. Geosci. Remote Sens.*, vol. 47, no. 2, pp. 481–493, Feb. 2009.

[10] F. Kugler, S. Lee, I. Hajnsek, and K. P. Papathanassiou, "Forest height estimation by means of pol-InSAR data inversion: The role of the vertical wavenumber," *IEEE Trans. Geosci. Remote Sens.*, vol. 53, no. 10, pp. 5294–5311, Oct. 2015.

[11] R. Guliaev, V. Cazcarra-Bes, M. Pardini, and K. Papathanassiou, "Forest height estimation by means of TanDEM-X InSAR and waveform LiDAR data," *IEEE J. Sel. Topics Appl. Earth Observ. Remote Sens.*, vol. 14, pp. 3084–3094, 2021.

[12] C. Choi et al., "Large-scale forest height mapping by combining TanDEM-X and GEDI data," *IEEE J. Sel. Topics Appl. Earth Observ. Remote Sens.*, vol. 16, pp. 2374–2385, 2023.

[13] Q. Zhang, L. Ge, S. Hensley, G. I. Metternicht, C. Liu, and R. Zhang, "PolGAN: A deep-learning-based unsupervised forest height estimation based on the synergy of PolInSAR and LiDAR data," *ISPRS J. Photogramm. Remote Sens.*, vol. 186, pp. 123–139, Apr. 2022.

[14] Y. Zhang et al., "Forest height estimation combining single-polarization tomographic and PolSAR data," *Int. J. Appl. Earth Observ. Geoinf.*, vol. 124, Nov. 2023, Art. no. 103532.

[15] W. Yang, S. Vitale, H. Aghababaei, G. Ferraioli, V. Pascazio, and G. Schirinzi, "A deep learning solution for height estimation on a forested area based on Pol-TomoSAR data," *IEEE Trans. Geosci. Remote Sens.*, vol. 61, 2023, Art. no. 5208214.

[16] L. Wang, J. Yang, L. Shi, P. Li, L. Zhao, and S. Deng, "Impact of backscatter in pol-InSAR forest height retrieval based on the multimodel random forest algorithm," *IEEE Geosci. Remote Sens. Lett.*, vol. 17, no. 2, pp. 267–271, Feb. 2020.

[17] W. Yang, S. Vitale, H. Aghababaei, G. Ferraioli, V. Pascazio, and G. Schirinzi, "A deep learning solution for height inversion on forested areas using single and dual polarimetric TomoSAR," *IEEE Geosci. Remote Sens. Lett.*, vol. 20, pp. 1–5, 2023.

[18] C. Xing, H. Wang, Z. Zhang, J. Yin, and J. Yang, "A review of forest height inversion by PolInSAR: Theory, advances, and perspectives," *Remote Sens.*, vol. 15, no. 15, p. 3781, Jul. 2023.

[19] G. Brigot, M. Simard, E. Colin-Koeniguer, and A. Boulch, "Retrieval of forest vertical structure from PolInSAR data by machine learning using LiDAR-derived features," *Remote Sens.*, vol. 11, no. 4, p. 381, Feb. 2019.

[20] J.-L. Bueso-Bello, D. Carcereri, M. Martone, C. González, P. Posovszky, and P. Rizzoli, "Deep learning for mapping tropical forests with TanDEM-X bistatic InSAR data," *Remote Sens.*, vol. 14, no. 16, p. 3981, Aug. 2022.

[21] D. Carcereri, P. Rizzoli, D. Ienco, and L. Bruzzone, "A deep learning framework for the estimation of forest height from bistatic TanDEM-X data," *IEEE J. Sel. Topics Appl. Earth Observ. Remote Sens.*, vol. 16, pp. 8334–8352, 2023.

[22] X. Wang and H. Wang, "Forest height mapping using complex-valued convolutional neural network," *IEEE Access*, vol. 7, pp. 126334–126343, 2019.

[23] H. Luo, C. Yue, F. Xie, B. Zhu, and S. Chen, "A method for forest canopy height inversion based on machine learning and feature mining using UAVSAR," *Remote Sens.*, vol. 14, no. 22, p. 5849, Nov. 2022.

[24] H. Luo, C. Yue, H. Yuan, N. Wang, and S. Chen, "A method for forest canopy height inversion based on UAVSAR and Fourier–Legendre polynomial—Performance in different forest types," *Drones*, vol. 7, no. 3, p. 152, Feb. 2023.

[25] X. Sun, B. Wang, M. Xiang, L. Zhou, S. Wang, and S. Jiang, "Machine-learning inversion of forest vertical structure based on 2-D-SGVBVoG model for P-band pol-InSAR," *IEEE Trans. Geosci. Remote Sens.*, vol. 60, 2022, Art. no. 5225115.

[26] G. E. Karniadakis, I. G. Kevrekidis, L. Lu, P. Perdikaris, S. Wang, and L. Yang, "Physics-informed machine learning," *Nature Rev. Phys.*, vol. 3, no. 6, pp. 422–440, May 2021.

[27] J. Armston et al., "AfriSAR: Gridded forest biomass and canopy metrics derived from LVIS, Gabon, 2016," Oak Ridge Nat. Lab. Distrib. Act. Arch. Center (ORNL DAAC), Oak Ridge, TN, USA, Tech. Rep. 1775, 2020, doi: 10.3334/ORNLDAAC/1775. [Online]. Available: https://daac.ornl.gov/cgi-bin/dsviewer.pl?ds_id=1775

[28] T. Fatoyinbo et al., "The NASA AfriSAR campaign: Airborne SAR and LiDAR measurements of tropical forest structure and biomass in support of current and future space missions," *Remote Sens. Environ.*, vol. 264, Oct. 2021, Art. no. 112533.

[29] P. A. Rosen et al., "Synthetic aperture radar interferometry," *Proc. IEEE*, vol. 88, no. 3, pp. 333–382, Mar. 2000.

[30] S. Cloude, *Polarisation: Applications in Remote Sensing*. Oxford, U.K.: Oxford Univ. Press, Oct. 2009, doi: 10.1093/acprof:oso/9780199569731.001.0001.

[31] M. Denbina, M. Simard, and B. Hawkins, "Forest height estimation using multibaseline PolInSAR and sparse LiDAR data fusion," *IEEE J. Sel. Topics Appl. Earth Observ. Remote Sens.*, vol. 11, no. 10, pp. 3415–3433, Oct. 2018.

[32] J. I. H. Askne, P. B. G. Dammert, L. M. H. Ulander, and G. Smith, "C-band repeat-pass interferometric SAR observations of the forest," *IEEE Trans. Geosci. Remote Sens.*, vol. 35, no. 1, pp. 25–35, Jan. 1997.

[33] H. A. Zebker and J. Villasenor, "Decorrelation in interferometric radar echoes," *IEEE Trans. Geosci. Remote Sens.*, vol. 30, no. 5, pp. 950–959, Sep. 1992.

[34] J. O. Hagberg, L. M. H. Ulander, and J. Askne, "Repeat-pass SAR interferometry over forested terrain," *IEEE Trans. Geosci. Remote Sens.*, vol. 33, no. 2, pp. 331–340, Mar. 1995.

[35] R. Bamler and P. Hartl, "Synthetic aperture radar interferometry," *Inverse Problems*, vol. 14, no. 4, pp. 1–55, Aug. 1998.

[36] F. Kugler, D. Schulze, I. Hajnsek, H. Pretzsch, and K. P. Papathanassiou, "TanDEM-X pol-InSAR performance for forest height estimation," *IEEE Trans. Geosci. Remote Sens.*, vol. 52, no. 10, pp. 6404–6422, Oct. 2014.

[37] M. Martone, B. Bräutigam, P. Rizzoli, C. Gonzalez, M. Bachmann, and G. Krieger, "Coherence evaluation of TanDEM-X interferometric data," *ISPRS J. Photogramm. Remote Sens.*, vol. 73, pp. 21–29, Sep. 2012.

[38] R. N. Treuhaft and P. R. Siqueira, "Vertical structure of vegetated land surfaces from interferometric and polarimetric radar," *Radio Sci.*, vol. 35, no. 1, pp. 141–177, Jan. 2000.

[39] A. Roueff, A. Arnaubec, P. C. Dubois-Fernandez, and P. Refregier, "Cramer–Rao lower bound analysis of vegetation height estimation with random volume over ground model and polarimetric SAR interferometry," *IEEE Geosci. Remote Sens. Lett.*, vol. 8, no. 6, pp. 1115–1119, Nov. 2011.

[40] S. R. Cloude, "Polarization coherence tomography," *Radio Sci.*, vol. 41, no. 4, pp. 1–27, Aug. 2006.

[41] S. R. Cloude, "Dual-baseline coherence tomography," *IEEE Geosci. Remote Sens. Lett.*, vol. 4, no. 1, pp. 127–131, Jan. 2007.

[42] M. Brolly, M. Simard, H. Tang, R. O. Dubayah, and J. P. Fisk, "A LiDAR-radar framework to assess the impact of vertical forest structure on interferometric coherence," *IEEE J. Sel. Topics Appl. Earth Observ. Remote Sens.*, vol. 9, no. 12, pp. 5830–5841, Dec. 2016.

[43] F. Chollet, *Deep Learning With Python*. Shelter Island, NY, USA: Manning, 2021.

Islam Mansour (Member, IEEE) received the B.Sc. degree in astronautical engineering from Istanbul Technical University (ITU), Istanbul, Turkey, in 2017, and the M.Sc. degree from Earth Oriented Space Science and Technology (ESPACE), Technical University of Munich (TUM), Munich, Germany, in 2021. He is currently pursuing the Ph.D. degree with the Swiss Federal Institute of Technology Zurich (ETH Zurich), Zürich, Switzerland.

From 2017 to 2019, he worked as a Systems and Software Engineer with the Chassis Systems Control division at Bosch, Budapest, Hungary, where he contributed to the Development of Automatic Parking Assistant Systems. From 2019 to 2020, he worked as a Student Assistant at TUM, focusing on algorithms for atmospheric drag estimation on CubeSats and exploring machine learning applications for remote sensing data. In July 2020, he joined the Polarimetric SAR Interferometry Research Group at the Microwaves and Radar Institute, German Aerospace Center (DLR), Oberpfaffenhofen, Germany, to conduct his master's thesis. Since March 2021, he has been conducting a Doctoral Research in the same group, specializing in physics-informed neural networks for synthetic aperture radar (SAR) applications, integrating physical modeling with machine learning techniques.

Konstantinos Papathanassiou (Fellow, IEEE) received the Dipl.Ing. and Ph.D. degrees from the Department of Physics, Technical University of Graz, Graz, Austria, in 1994 and 1999, respectively.

From 1992 to 1994, he was with the Institute for Digital Image Processing (DIBAG), Joanneum Research, Graz. From 1995 to 1999, he was with the Microwaves and Radar Institute (HR), German Aerospace Center (DLR), Oberpfaffenhofen, Germany. From 1999 to 2000, he was an EU Post-Doctoral Fellow with the Applied Electromagnetics (AEL), St. Andrews, U.K. Since October 2000, he has been a Senior Scientist with the Microwaves and Radar Institute (HR), DLR, leading the Information Retrieval Research Group. He has authored or co-authored more than 60 peer-reviewed articles in international journals and more than 300 contributions in international conferences and workshops. His main research interests include polarimetric and interferometric processing and calibration techniques, polarimetric SAR interferometry, and quantitative parameter estimation from SAR data, as well as in SAR mission design and SAR mission performance analysis.

Dr. Papathanassiou is a member of the DLR's TanDEM-X and Tandem-L Science Teams, JAXA's ALOS-PalSAR Cal-Val Teams, ESA's BIOMASS Mission Advisory Group, JAXA's Carbon and Kyoto Initiative, and NASA's GEDI Mission Science Team. He was a recipient of the IEEE Geoscience and Remote Sensing Society (GRSS) International Geoscience and Remote Sensing Symposium (IGARSS) Prize Paper Award in 1998, the Best Paper Award of the European SAR Conference (EUSAR) in 2002, the IEEE GRSS J-STARS Paper Award in 2019, the DLR Science Award in 2002 and 2020, the DLR's Senior Scientist Award in 2011, and the DLR's Otto Lilienthal Award in 2020.

Ronny Hänsch (Senior Member, IEEE) received the Diploma degree in computer science and the Ph.D. degree from the TU Berlin, Berlin, Germany, in 2007 and 2014, respectively.

He is a currently a Senior Scientist with the Microwave and Radar Institute, German Aerospace Center, Cologne, Germany, where he leads the Machine Learning Team in the Signal Processing Group, SAR Technology Department. He continues to lecture with the Computer Vision and Remote Sensing Group, TU Berlin. His research interests include computer vision and machine learning with a focus on remote sensing (in particular SAR processing and analysis).

Dr. Hänsch served as a (co-)chair of the IEEE GRSS Image Analysis and Data Fusion Technical Committee from 2017 to 2023 and has been serving as the co-chair of the ISPRS working group on Image Orientation and Sensor Fusion since 2016. He co-organizes the CVPR Workshop EarthVision and the IGARSS Tutorial on Machine Learning in Remote Sensing since 2017. He has extensive experience in organizing remote sensing community competitions and serves as the Geoscience and Remote Sensing Society (GRSS) representative within SpaceNet, where he was the Technical Lead of the SpaceNet eight Challenge. He served as the Editor for the GRSS eNewsletter from 2021 to 2024 and is the Editor in Chief of the Geoscience and Remote Sensing Letters since 2024.

Irena Hajnsek (Fellow, IEEE) received the Dipl. degree (Hons.) in fluvial river systems from the Free University of Berlin, Berlin, Germany, in 1996, and the Dr. rer. nat. degree (Hons.) in model-based estimation of soil moisture from fully polarimetric synthetic aperture radar from the Friedrich Schiller University of Jena, Jena, Germany, in 2001.

Since November 2009, she has been a Professor of Earth Observation with the Swiss Federal Institute of Technology (ETH) Zürich Institute of Environmental Engineering, Zürich, Switzerland, and at the same time the Head of the Polarimetric SAR Interferometry Research Group, German Aerospace Center Microwaves and Radar Institute, Weßling, Germany. Since 2010, she has been with the Science Coordinator of German Satellite Mission TanDEM-X. Her main research interests include electromagnetic propagation and scattering theory, radar polarimetry, SAR and interferometric SAR data processing techniques, and environmental parameter modeling and estimation.

Dr. Hajnsek was a member of IEEE GRSS AdCom, from 2013 to 2021. She is a member of European Space Agency Mission Advisory Group for the ROSE-L Mission. She has been awarded with the Doctor degree honoris causa from the University of Oslo, Oslo, Norway, for her outstanding contributions to science, including the development of algorithms using innovative radar techniques for environmental parameter estimation and setting requirements for the design of future radar missions in application areas as permafrost, glaciers, disaster management, agriculture, and climate change impacts, in 2024. She was the Technical Program Co-Chair of the IEEE IGARSS 2012 in Munich, Germany, and 2019 in Yokohama, Japan. She was the Vice President of the IEEE GRSS Technical Committees, from 2016 to 2020. She has been the Founder of the New Technical Committee Remote Sensing Environment, Analysis and Climate Technologies (REACT), which exists, since November 2021.